Earth and Planetary Science Letters 368 (2013) 78–87

Contents lists available at SciVerse ScienceDirect

Earth and Planetary Science Letters

journal homepage: www.elsevier.com/locate/epsl

The effect of methane hydrate morphology and water saturation on seismic wave attenuation in sand under shallow sub-seafloor conditions

Angus I. Best [a,*], Jeffrey A. Priest [b], Christopher R.I. Clayton [b], Emily V.L. Rees [b]

[a] National Oceanography Centre, University of Southampton Waterfront Campus, European Way, Southampton SO14 3ZH, United Kingdom
[b] Faculty of Engineering and the Environment, University of Southampton, Highfield, Southampton SO17 1BJ, United Kingdom

ARTICLE INFO

Article history:
Received 26 April 2012
Received in revised form
25 February 2013
Accepted 27 February 2013
Editor: P. Shearer
Available online 29 March 2013

Keywords:
seismic attenuation
hydrate
sediment
morphology

ABSTRACT

A better understanding of seismic wave attenuation in hydrate-bearing sediments is needed for the improved geophysical quantification of seafloor methane hydrates, important for climate change, geohazard and economic resource assessment. Hence, we conducted a series of small strain ($<10^{-6}$), seismic frequency (50–550 Hz), laboratory resonant column experiments on synthetic methane hydrate-bearing sands under excess-water seafloor conditions. The results show a complex dependence of P- and S-wave attenuation on hydrate saturation and morphology. P- and S-wave attenuation in excess-water hydrate-bearing sand is much higher than in excess-gas hydrate-bearing sand and increases with hydrate saturation between 0 and 0.44 (the experimental range). Theoretical modelling suggests that load-bearing hydrate is an important cause of heightened attenuation for both P- and S-waves in gas and water saturated sands, while pore-filling hydrate also contributes significantly to P-wave attenuation in water saturated sands. A squirt flow attenuation mechanism, related to microporous hydrate and low aspect ratio pores at the interface between sand grains and hydrate, is thought to be responsible for the heightened levels of attenuation in hydrate-bearing sands at low hydrate saturations (<0.44).

1. Introduction

Detection and quantification of seabed methane is important for predicting greenhouse gas fluxes between the seabed, the water column and the atmosphere and their impact on future climate change. The highest concentrations of seabed methane are thought to occur in association with seabed methane hydrates that are especially sensitive to global warming in polar regions. Methane hydrates are ice-like compounds of methane and water that are stable at water depths greater than about 300 m for typical seafloor temperatures of 4 °C; perturbations in bottom water temperature can cause hydrates to dissociate and release methane gas into the water column (Westbrook et al., 2009). Methane gas and methane hydrate quantification techniques are also needed for assessing seafloor geohazards (e.g., landslides associated with hydrate dissociation on continental slopes) and hydrate energy resources (hydrate reservoir characterisation) (Riedel et al., 2010).

Seismic geophysical methods can be used to image and quantify gas hydrates and free gas in sediments (Ecker et al., 1998, 2000; Guerin and Goldberg, 2002; Matsushima, 2006; Pratt et al., 2005; Riedel et al., 2010; Westbrook et al., 2008; Wood et al., 2000) given suitable knowledge of how seismic velocity and attenuation relate to hydrate content and morphology, and sediment type (Chand et al., 2006; Lee, 2002; Waite et al., 2010; Yun et al., 2005). However, the interpretation of in situ seismic attenuation measurements is uncertain because of our limited understanding of attenuation mechanisms in sediments in general, and the role of hydrate in particular. It is often difficult to unambiguously relate attenuation measurements from seismic surveys and sonic well logs to specific hydrate or sediment conditions because of spatial averaging effects, so laboratory studies are more suitable in this respect. However, given a uniform sediment sample, isolating intrinsic loss mechanisms and accurately predicting their dependence on, for example, measurement frequency, effective pressure, temperature, pore fluid type and saturation, hydrate saturation and morphology, are major challenges.

In this paper, we present novel, laboratory resonant column results for seismic compressional and shear wave attenuation measured in water saturated, synthetic methane hydrate-bearing sand created under excess-water conditions at an effective pressure of 500 kPa and a temperature of 10 °C, representative of shallow sub-seabed hydrates. The results show that attenuation is significantly higher than that observed by Priest et al. (2006) in methane gas saturated, methane hydrate-bearing sand

* Corresponding author. Tel.: +44 23 8059 6577; fax: +44 23 8059 6554.
E-mail address: angus.best@noc.ac.uk (A.I. Best).

0012-821X
http://dx.doi.org/10.1016/j.epsl.2013.02.033

where the hydrate was created under excess-gas conditions using the same apparatus. In an attempt to study the possible contribution of different hydrate morphologies to intrinsic attenuation, we introduce the Hydrate Effective Grain (HEG) model based on the notion of microporous hydrate grains. Comparison with the resonant column observations suggests that the amount of load-bearing hydrate in particular is an important control on P- and S-wave attenuation, while pore-filling hydrate also affects P-wave attenuation in water saturated sands.

2. Experiments

2.1. Gas hydrates resonant column

We performed a series of laboratory experiments on Leighton Buzzard sand specimens (7 cm diameter, 14 cm high solid cylinders) using the gas hydrates resonant column (GHRC) developed in Southampton, United Kingdom. Previous studies focused on methane saturated, synthetic methane hydrate-bearing sand prepared using the excess gas method (Best et al., 2010; Clayton et al., 2005; Priest, 2004; Priest et al., 2005, 2006). Here, we present new data for water saturated, synthetic methane hydrate-bearing sand prepared using the excess water method as described in Clayton et al. (2010), Priest et al. (2009) and Rees (2009).

The main advantage of the resonant column method for elastic wave propagation studies is that it enables all four seismic parameters of interest (V_p, V_s, Q_p^{-1}, Q_s^{-1}) to be measured at similar frequencies (50–550 Hz) to those used during in situ seismic surveys. Here, V_p and V_s are the body wave P- and S-wave velocities, respectively, and Q_p^{-1} and Q_s^{-1} are the P- and S-wave attenuations (inverse quality factors Q_p, Q_s), respectively. All measurements were conducted in a temperature-controlled cell under a simulated hydrostatic effective stress of 500 kPa with a pore fluid pressure of 15 MPa and a temperature of 10 °C. The specimens were excited in torsional and longitudinal flexural resonance by sweeping the drive frequency around the specimen fundamental mode frequencies and monitoring the resultant vibration amplitude via an accelerometer attached to the drive mechanism mounted on the top of the specimen.

The torsional and longitudinal flexural specimen velocities were calculated from the observed resonant frequencies along with knowledge of the specimen size and mass, and mass polar moment of inertia of the top cap. Shear and Young's moduli can be derived from the velocities and the calculated specimen density. The P-wave modulus and bulk modulus were then derived using well-known relationships (Birch, 1961). Attenuation was measured for both excitation modes from the free vibration amplitude decay curve after the power to the drive system was turned off (Priest et al., 2006). Attenuation was first measured as the logarithmic decrement, then converted into quality factor Q and the specific dissipation function Q^{-1}. Knowledge of the torsional (shear modulus) and longitudinal flexural (Young's modulus) attenuations allowed derivation of the P-wave and bulk modulus attenuations using relationship given by Eqs. (1)–(3) in Winkler and Nur (1979).

A particular feature of the resonant column configuration is that, using the torsional and longitudinal flexural modes, it is only possible to measure the frame elastic moduli of a porous medium with significant permeability like sand specimens. That is, even in the case of a water saturated specimen, only the velocities and elastic moduli associated with the solid framework of mineral grains are measured. Both vibration modes involve no volume change in the bulk specimen, so it is impossible to measure directly the compressional wave properties of the bulk system of fluid and framework of solid mineral grains. Although this adds complexity to the interpretation, the results are still useful as will be shown below. Although the measured resonant column attenuations are partly caused by global viscous fluid flow between the fluid and frame, the direction of fluid flow is particular to the resonance modes. While this is equivalent for torsional vibration in the resonant column and for shear (S) body waves in the Earth, the same cannot be said for longitudinal flexural vibration in the resonant column and for compressional (P) body waves. For the flexural mode, the fluid flow is perpendicular to the wave propagation direction (see Fig. 1), while it is parallel with the wave propagation direction for P-waves. However, we take these attenuations to be equivalent if we assume the sand specimens are homogeneous and isotropic. What is important is the observed magnitude of attenuation due to average fluid flow in the bulk sand specimens under frame shear and longitudinal flexural vibration. Also, any local viscous fluid flow mechanism will be relatively unaffected by the macroscopic (global) fluid flow.

2.2. Methane hydrate formation, morphology and seismic velocity

Methane hydrate was formed in the sand specimens using two methods: excess gas (Priest et al., 2005) and excess water (Priest et al., 2009). The excess gas method involves distributing a known mass of water throughout the sand specimen, saturating the partially water saturated sand with methane gas, then taking the specimen into the hydrate stability field. The velocity and elastic moduli results indicated a grain cementing hydrate morphology that led to a rapid increase in velocity with hydrate saturation up to about 5%, as reported in Clayton et al. (2005) and Priest et al. (2005). Water tends to coat the water–wet sand grains and so the methane reacts with the water to form grain-coating hydrate, a proportion of which acts to cement the grains at grain contacts (Chand et al., 2006). By contrast, the excess water method involves injecting methane gas into the specimen and then flooding the sand specimen with water before taking the specimen into the hydrate stability field. This is thought to produce a pore-filling hydrate morphology as the methane gas

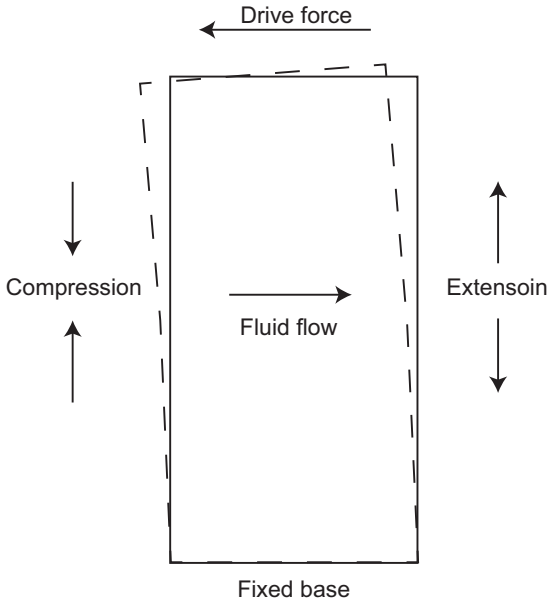

Fig. 1. Diagram showing the direction of fluid flow in a porous sand specimen during longitudinal flexural excitation inside the resonant column. The solid framework of mineral grains undergoes compression and extension while the saturating fluid flows horizontally from the side under compression to the side under extension.

tends to distribute itself in the pore space of the sand, surrounded by the water which naturally adheres to the water–wet sand grains. This interpretation is supported by the velocity and elastic moduli results reported respectively in Priest et al. (2009) and in Clayton et al. (2010) which show only slight increases with hydrate saturation.

2.3. Resonant column attenuation results

A total of six separate, excess water, experiments were performed to give attenuation results for water saturated sand specimens at hydrate saturations S_h=0, 0.08, 0.13, 0.19, 0.32 and 0.44 shown in Fig. 2a for P-waves (Q_p^{-1}) and in Fig. 2b for S-waves (Q_s^{-1}); the effective pressure was 500 kPa (pore fluid pressure 15 MPa) and the temperature was 10 °C.

Overall, both Q_p^{-1} and Q_s^{-1} increase with hydrate saturation S_h with Q_p^{-1} (maximum value 0.102) being about double the size of Q_s^{-1} (maximum value 0.050). Also, both Q_p^{-1} and Q_s^{-1} show two attenuation maxima, at S_h=0.13 and S_h=0.32. The increase in attenuation with S_h and the attenuation maxima are significant relative to the experimental errors of ± 20%. The errors are based on the maximum 95% confidence limits for a range of calibration experiments on standard materials, from fitting least squares regression curves to the free vibration decay amplitudes with time (see Priest, 2004). When compared to the excess gas (gas saturated) attenuation results from Priest et al. (2006), also shown in Fig. 2, the excess water attenuations are generally much higher, both for Q_p^{-1} and Q_s^{-1}. Both the excess gas and excess water attenuations are larger than the attenuation in partially water saturated sand (no hydrate) from Priest et al. (2006).

These results are unexpected because of: (i) the presence of attenuation maxima (one for excess gas hydrate, two for excess water hydrate); and (ii) the relative magnitudes of attenuation in water and gas saturated, hydrate-bearing sand formed under different conditions. However, without a suitable theoretical model to explain the shape of the attenuation curves, it is difficult to draw conclusions about the veracity of the results. Moreover, it is difficult to assess their applicability to seafloor hydrates that in general will not conform to the specific conditions of saturation state and measurement frequency of these laboratory observations, as well as lithological variations (e.g., clay content).

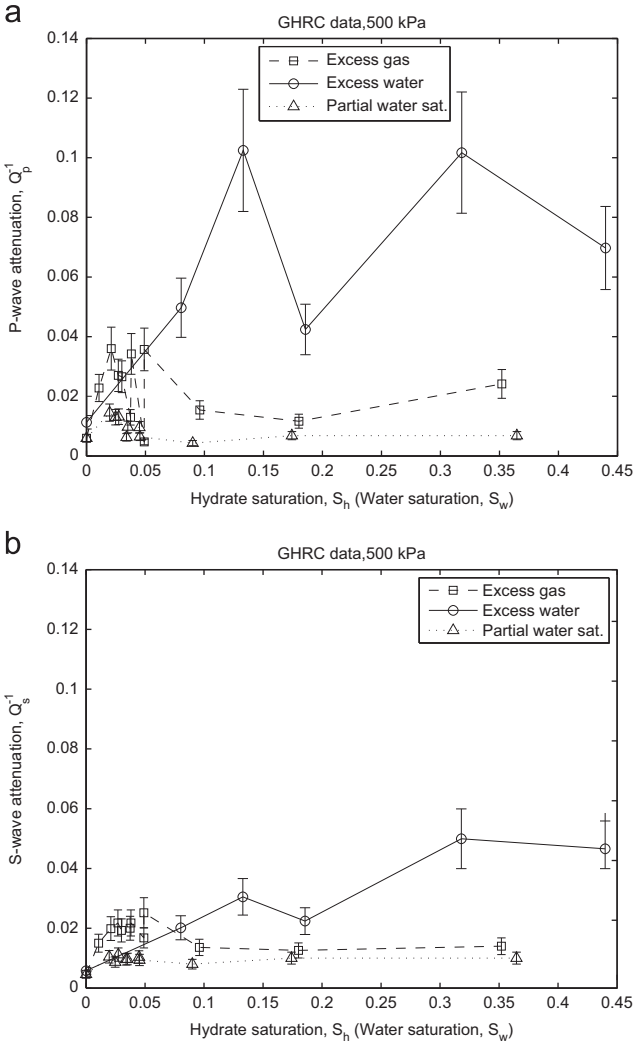

Fig. 2. Experimental attenuation results for (a) P-waves (Q_p^{-1}) and (b) S-waves (Q_s^{-1}) for methane hydrate-bearing sand from the Gas Hydrate Resonant Column. Hydrate was created using the excess gas method (dashed line; data from Priest et al. (2006)) and the excess water method (solid line; new data). Also shown are the results from the excess gas experiments after the hydrate was allowed to dissociate (dotted line; data from Priest et al. (2006)) for which the *x*-axis is equivalent to water saturation, S_w.

3. Theory

3.1. Hydrate effective grain (HEG) model

Here, we extend the Ecker et al. (1998) and Ecker et al. (2000) theoretical approaches, that were used to explain the effect of grain cementing, load-bearing and pore-filling hydrate morphologies on seismic velocities, to account for seismic wave attenuation. Firstly, let us consider the likely causes of elevated intrinsic attenuation in sediments due to hydrate. Unlike early concepts of hydrate acting to stiffen sediments and reduce attenuation (Dvorkin et al., 2003), laboratory and in situ studies consistently show that the presence of hydrate leads to elevated elastic wave attenuation (Dvorkin and Uden, 2004; Guerin and Goldberg, 2002; Matsushima, 2006; Pratt et al., 2005; Priest et al., 2006), also shown in this study (Fig. 2). Kuhs et al. (2004) showed the microporous structure of natural hydrates, observed the same structures in synthetic hydrates formed under similar conditions in the laboratory, and suggested that this could give rise to heightened attenuation in sediments. With this in mind, hydrate grains could be thought of as a compliant material with inclusions of gas or water, rather than as a solid mineral. The inclusions are a consequence of isolated pockets of gas or water trapped during hydrate formation either under excess-gas or excess-water conditions. In this case, hydrate could behave in a similar fashion to other microporous, compliant minerals in sediments and rocks, such as clay minerals (Best and McCann, 1995; Leurer, 1997; Marketos and Best, 2010), in causing local viscous fluid flow (squirt flow).

Ecker et al. (2000) gave expressions for the frame bulk and shear modulus (respectively K_b and G_b) for load-bearing and pore-filling hydrate, based on the theory of Dvorkin et al. (1999) for clay-rich marine sediments; the Ecker et al. (1998) frame moduli expressions for grain cementing hydrate were based on the theory of Dvorkin et al. (1994). Instead of inputting these frame moduli values into the Gassmann (1951) model to calculate seismic velocities in fluid saturated sediments as they do, we pass them to the Biot poroelastic theoretical model (Biot, 1956a,b; Mavko et al., 1998) to predict frequency-dependent P- and S-wave velocities and attenuations. In addition, to account for squirt flow associated with the microporous hydrate grains, we make the frame elastic moduli both complex and frequency-dependent using the Effective Grain Model (EGM) approach of Leurer (1997) and Leurer and Brown (2008), who used it to

describe clay-squirt flow in marine sediments. Here, the bulk and shear moduli of the solid hydrate phase (K_h, G_h) in the Ecker et al. (1998) and Ecker et al. (2000) expressions are substituted by those of effective grains of hydrate with fluid inclusions ($\hat{K}_h$, $\hat{G}_h$).

There are several ways to introduce fluid inclusions into the effective hydrate grains (Berryman, 1995). Wu (1966) derived exact expressions for ellipsoidal inclusions as well as approximate expressions for the special cases of disk-shaped (aspect ratio $\varepsilon=0$) and spherical ($\varepsilon=1$) inclusions. Walsh (1969) noted that Wu's expressions for disk-shaped inclusions are only valid for aspect ratios much less than G_i/G_h where G_i and G_h are the shear moduli of the inclusion and host material, respectively; this means in practice that G_i must be significantly greater than zero for aspect ratios of interest here ($<10^{-3}$ for microcracks in sediments and rocks). Walsh (1969) gave alternative expressions for penny-shaped, fluid inclusions that are valid for $G_i=0$ and small aspect ratios $\varepsilon \leq 10^{-3}$. The choice of fluid inclusion shape is somewhat arbitrary, and leads to different results (see Section 3.2).

We follow the scheme of Johnston et al. (1979) to make the hydrate effective grain moduli both frequency-dependent and complex ($\hat{K}_h(f)$, $\hat{G}_h(f)$; see Fig. 3) using the correspondence principle. This is achieved by introducing complex, frequency dependent elastic moduli of the inclusion material ($(\hat{K}_i(f), \hat{G}_i(f))$ here taken as water or methane),

$$\hat{K}_i(f) = K_i + i\omega\gamma \tag{1}$$

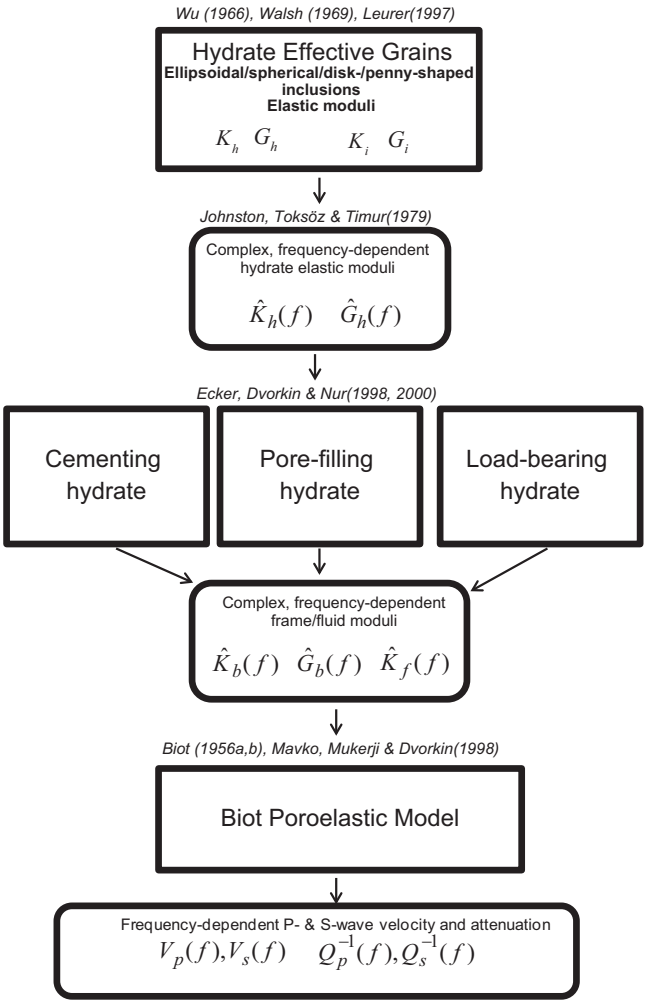

Fig. 3. Overview of the poro-viscoelastic Hydrate Effective Grain (HEG) model.

and

$$\hat{G}_i(f) = G_i + i\omega\eta, \tag{2}$$

where K_i is the inclusion bulk modulus, G_i is the inclusion shear modulus (0 for water or gas), ω is angular frequency ($=2\pi f$ where f is frequency), and η is inclusion viscosity. The parameter γ is given by the expression

$$\gamma = \tau K_h = \frac{3\eta}{2\varepsilon^2 \Re(\hat{K}_i)} K_h, \tag{3}$$

where K_h is the solid hydrate (host material) bulk modulus, τ is the relaxation time of the viscous loss mechanism, and ε is the fluid inclusion aspect ratio (see Johnston et al., 1979; Leurer and Brown, 2008). The full expressions for the effective hydrate grain elastic moduli $\hat{K}_h(f)$ and $\hat{G}_h(f)$ are given by Eqs. (12) and (13) of Leurer and Brown (2008); they include terms that depend on inclusion shape (see discussion on choice of inclusion shape above). The purpose of these shape terms is to relate the uniform strain field at infinity to the local strain field around a fluid inclusion. The expressions for $\hat{K}_h(f)$ and $\hat{G}_h(f)$ can be extended to include a distribution of aspect ratios, but here we will consider a single aspect ratio for simplicity.

The resulting model, here called the Hydrate Effective Grain (HEG) model, allows frequency-dependent velocity and attenuation to be calculated as a function of hydrate saturation, hydrate morphology (grain cementing, load-bearing or pore-filling), and water saturation S_w (where $S_w+S_g=1$ for methane gas saturation S_g). Note that the inclusion fluid was taken as either 100% water or 100% methane saturated; partial saturation S_w refers to the fluid saturation of the macropores in the sand/hydrate grain framework only. A summary of the HEG model steps is given in Fig. 3.

Some model input parameter choices must be made, given in Table 1. The grain coordination number (a measure of the number of contacts per grain in a grain pack) was adjusted to give a reasonable fit to the measured velocities (Priest et al., 2005, 2009); hence, the grain coordination number of $n=4$ in Table 1 differs from the usually accepted value of 8–9 for grain packs. A critical porosity of 0.38 was used for the densely packed sand used in the experiments, with an actual sand pack porosity of 0.42 used throughout. Water saturation S_w was taken as 0.01 for the excess-gas experiments, equivalent to the estimated amount of bound water. The main free parameters were inclusion aspect

Table 1
List of HEG model input parameters.

Parameter	Symbol	Value	Units
Temperature	T	10.0	°C
Pore fluid pressure	P_p	15.0×10^6	Pa
Effective pressure	P_{eff}	5×10^5	Pa
Quartz bulk modulus	K_q	36.5×10^9	Pa
Quartz shear modulus	G_q	45.0×10^9	Pa
Quartz density	ρ_q	2650	kg m^{-3}
Hydrate bulk modulus	K_h	7.9×10^9	Pa
Hydrate shear modulus	G_h	3.3×10^9	Pa
Hydrate density	ρ_h	910	kg m^{-3}
Water bulk modulus	K_w	2.17×10^9	Pa
Water density	ρ_w	1006	kg m^{-3}
Methane bulk modulus	K_g	51.858	Pa
Methane density	ρ_g	0.1334	kg m^{-3}
Water viscosity	η_w	1.0×10^{-3}	Pa s
Porosity	φ	0.42	
Critical porosity	φ_0	0.38	
Grain coordination number	n	4.0	Dimensionless
Grain diameter	d	100×10^{-6}	m
Bulk permeability (load-bearing)	κ	10.0×10^{-15}	m^2
Bulk permeability (pore-filling)	κ	100.0×10^{-15}	m^2

ratio ε, inclusion volume concentration in the hydrate S_i, and sediment permeability. For simplicity, permeability was estimated to be 10 mD for excess-gas hydrate that is expected to block pore throats to a certain degree, and 100 mD for pore-filling hydrate that is expected to have a smaller pore throat blocking effect; the clean sand without hydrate is estimated to have a permeability of the order of 1 Darcy (1.0×10^{-12} m^2). In fact, attenuation at 200 Hz is insensitive to permeability; permeability controls the global fluid flow (Biot) relaxation frequency, not the squirt flow characteristic frequency associated with the microporous grains. Water inclusions with a viscosity of 1 cP (1.0×10^{-3} Pa s) were chosen for both hydrate morphologies (gas inclusions were found to give negligible attenuations and are not considered further).

3.2. HEG model results

We found that the cementing hydrate HEG model gave negligible attenuation and is not considered further here. We also found that, using penny-shaped, water-filled inclusions according to Walsh (Eqs. (1a) and (1b) in Walsh, 1969) gave similar attenuation magnitudes to the observations, but no attenuation peaks. However, the pore-filling hydrate HEG model could only explain elevated P-wave attenuation under water saturated conditions (it predicts zero S-wave attenuation), while the load-bearing HEG model predicted elevated attenuation for both P- and S-waves. The results for spherical inclusions gave negligible attenuation.

The main result of interest here is that a hybrid HEG model was found to predict attenuation peaks of the right magnitude. If the expressions for disk-shaped inclusions (that relate the uniform strain field at infinity to the local strain field around an inclusion) by Wu (Eqs. (8), (9), (23) and (24) in Wu, 1966) (i.e., aspect ratio $\varepsilon=0$) are used in combination with a finite aspect ratio (relating to the viscous loss relaxation time) in Eqs. (1)–(3), then this hybrid model gives attenuation peaks that are sensitive to S_i and ε, as illustrated in Fig. 4 for water saturation $S_w=0.01$and in Fig. 5 for $S_w=1.0$ (note different ordinate scales). So the hybrid model approximates the elastic strain field at infinity based on zero aspect ratio, disk-like inclusions, yet at the same time calculates the viscous (local flow) losses using a finite inclusion aspect ratio. We interpret this hybrid model as equivalent to hydrate grains with isolated, extremely low aspect ratio inclusions ($\varepsilon\to0$) that do not contribute to squirt flow attenuation (only to the effective elastic moduli), and finite aspect ratio inclusions at the edges of the hydrate grains that are connected to the large pores of the sand pack and hence give rise to squirt flow attenuation ($\varepsilon\sim10^{-4}$ for attenuation peaks at seismic frequencies). However, as noted in Section 3.1, disk-shaped inclusions are only valid for a significantly large inclusion shear modulus. In fact, we found that changing the value of G_i up to $\sim10^6$ Pa gave identical results to those given in Figs. 4 and 5 (keeping the inclusion viscosity equal to that of water).

Figs. 4 and 5 illustrate the main features of the hybrid HEG model predictions (hereafter referred to as simply the HEG model) for load-bearing hydrate. For gas saturated ($S_w=0.01$),

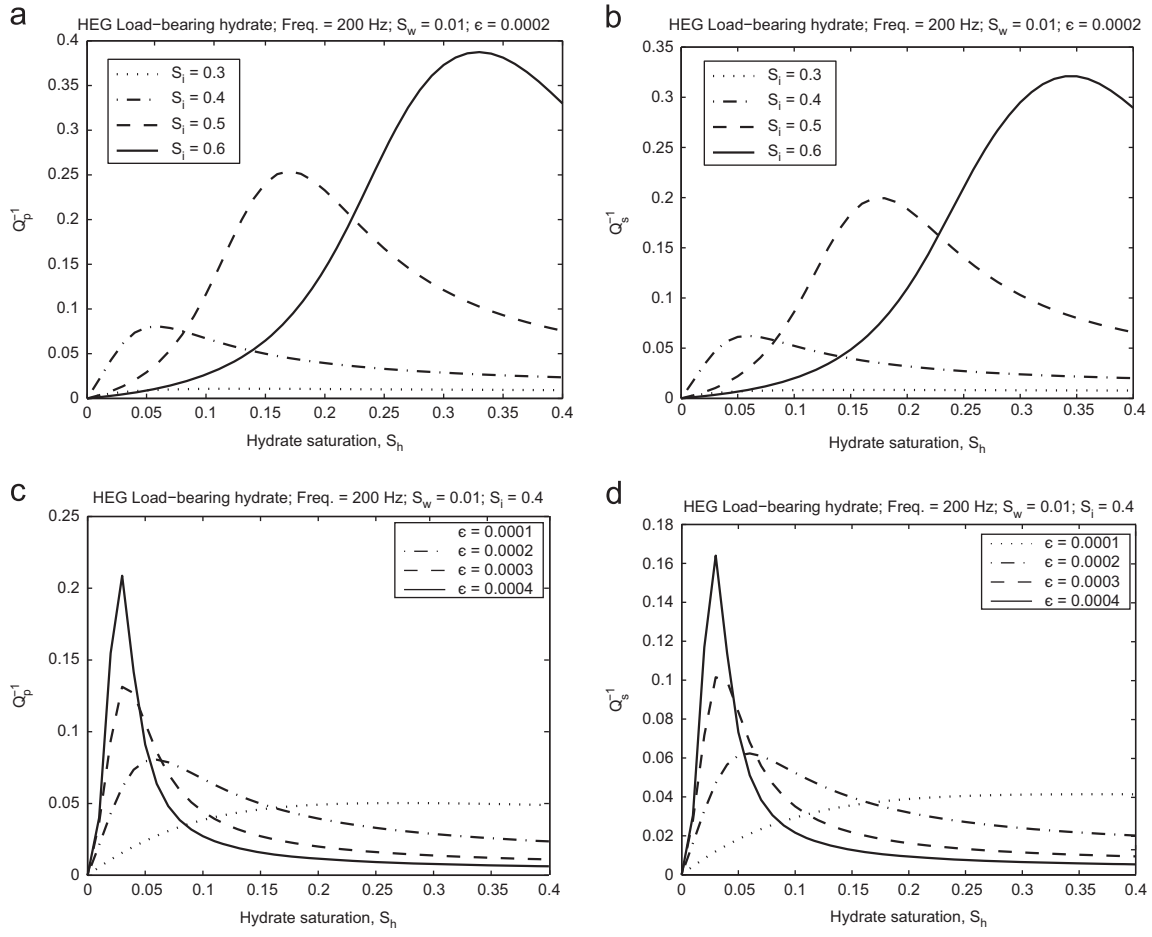

Fig. 4. HEG model results for disk-shaped inclusions according to Wu (1966) and load-bearing hydrate at a frequency of 200 Hz and water saturation $S_w=0.01$ (dry). Attenuation for (a and c) P-waves (Q_p^{-1}) and (b and d) S-waves (Q_s^{-1}) versus hydrate saturation S_h as a function of: (a and b) hydrate grain fluid inclusion concentration S_i for an inclusion aspect ratio $\varepsilon=2.0\times10^{-4}$; and (c and d) hydrate grain inclusion aspect ratio ε for an inclusion concentration $S_i=0.4$.

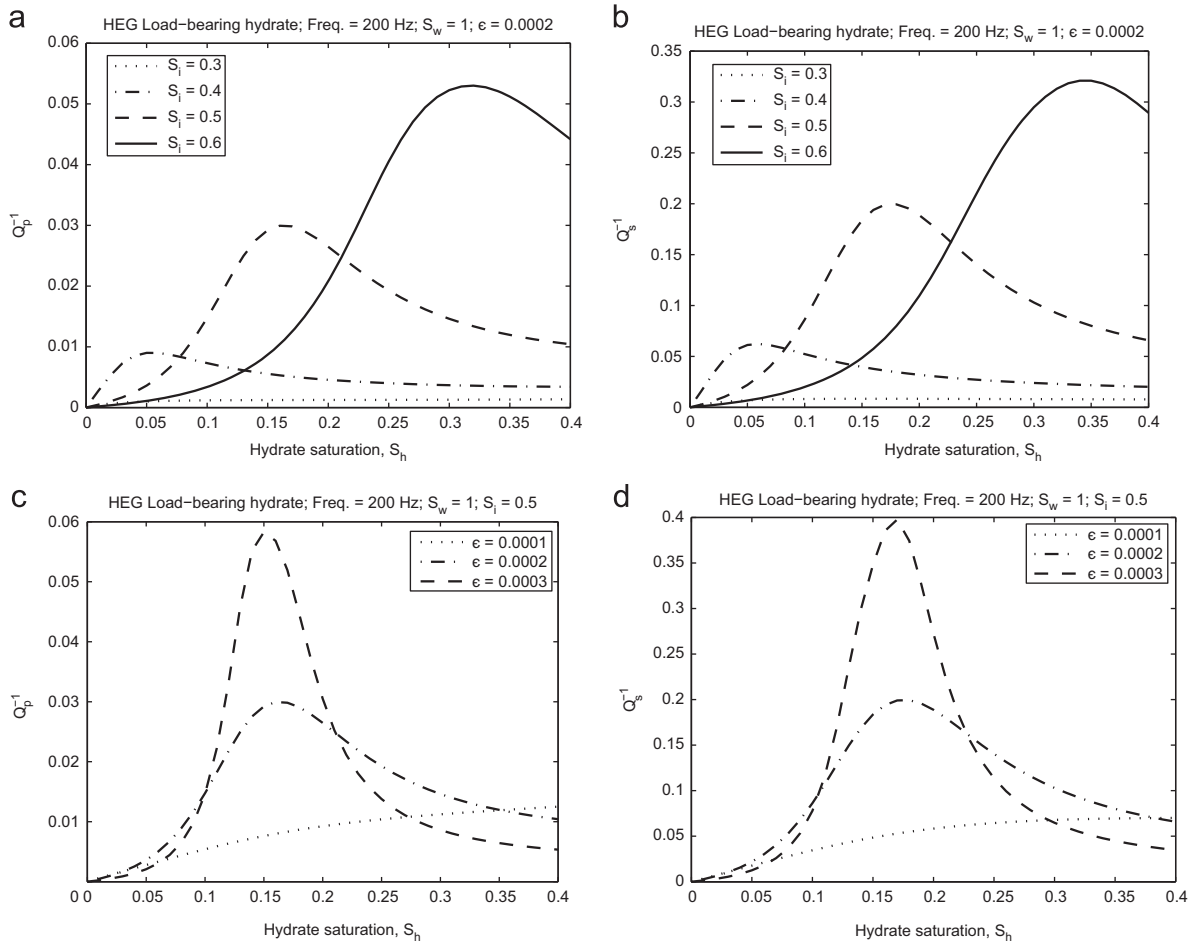

Fig. 5. HEG model results for disk-shaped inclusions according to Wu (1966) and load-bearing hydrate at a frequency of 200 Hz and $S_w=1.0$ (wet). Attenuation for P-waves Q_p^{-1} (a and c) and S-waves Q_s^{-1} (b and d) versus hydrate saturation S_h as a function of: (a and b) hydrate grain fluid inclusion concentration S_i for $\varepsilon=2.0\times10^{-4}$; and (c and d) hydrate fluid inclusion aspect ratio ε for $S_i=0.5$.

hydrate-bearing sand, Q_p^{-1} and Q_s^{-1} are shown as a function of inclusion concentration $S_i=0.3$, 0.4, 0.5 and 0.6 for a constant inclusion aspect ratio $\varepsilon=2.0\times10^{-4}$ (Fig. 4a and b), and as a function of inclusion aspect ratio $\varepsilon=1.0\times10^{-4}$, 2.0×10^{-4}, 3.0×10^{-4} and 4.0×10^{-4} for a constant $S_i=0.4$ giving rise to an attenuation peak at about $S_h=0.05$ (Fig. 4c and d). It appears that S_i controls the position of the attenuation peak with respect to hydrate saturation S_h, while ϵ controls the size of the attenuation peak (for a given frequency). The predicted Q_p^{-1} values are slightly larger than the predicted Q_s^{-1} values for a given hydrate saturation. Fig. 5 shows similar results for water saturated ($S_w=1.0$), hydrate-bearing sand, except that Fig. 5c and d show how an attenuation peak at $S_h=0.15$ can be predicted for $S_i=0.5$ and $\varepsilon=1.0\times10^{-4}$, 2.0×10^{-4} and 3.0×10^{-4}. A major difference between Figs. 4 and 5 is that the predicted Q_p^{-1} is much smaller than Q_s^{-1} for water saturated sand $S_w=1.0$ (again, note change of ordinate scales in Figs. 4 and 5).

Despite these model peculiarities, we attempted to fit the HEG model curves to the attenuations observed in the GHRC. Fig. 6a compares the GHRC data with HEG model curves for pore-filling hydrate and two different combinations of S_i and ε for load-bearing hydrate, together with the cumulative attenuation from all three mechanisms. The cumulative attenuation is simply the sum of the attenuations (Q^{-1}) from each mechanism (pore-filling, load-bearing with different values of S_i, ε). This is similar to adding the attenuation contributions for each inclusion aspect ratio in a distribution of aspect ratios (each aspect ratio has its own concentration) as in Leurer and Brown (2008). The model parameters were: for pore-filling hydrate, $S_i=0.36$ and $\varepsilon=1.0\times10^{-4}$; for the two load-bearing hydrate models $S_i=0.42$, 0.48 and $\varepsilon=6.0\times10^{-4}$, 3.0×10^{-4} respectively; the pore-filling hydrate proportion was set at 0.2 of S_h, while the load-bearing hydrate proportions were each set at 0.4 of S_h. Note that the pore-filling hydrate HEG model predicts a monotonically increasing Q_p^{-1} with S_h over which the Q_p^{-1} peaks from the load-bearing HEG model are superimposed, giving good agreement with the observed P-wave attenuations. This exercise shows that it is feasible to match the two Q_p^{-1} peaks seen on the GHRC data with some arbitrary combination of load-bearing and pore-filling hydrate HEG models with realistic inclusion aspect ratios of about 10^{-4}. In Fig. 6, we show the model predictions for hydrate saturation up to $S_h=1.0$ for completeness, although the GHRC observations only go up to $S_h=0.44$. Fig. 6b shows the HEG model results for Q_s^{-1}, based on the best fit to Q_p^{-1} shown in Fig. 6a; here, the HEG model Q_s^{-1} predictions are much too high compared to the GHRC observations.

Fig. 6c and d show the best HEG model fits to the Q_s^{-1} data for water saturated conditions. It was not possible to get an exact fit to the Q_s^{-1} peaks, but the cumulative curve gives a good estimate of the overall trend (note that pore-filling hydrate gives zero contribution to Q_s^{-1}). Fig. 6e and f show the HEG model results for gas saturated conditions ($S_w=0.01$); all other model input parameter were kept the same as in Fig. 6c and d, except that only a single load bearing aspect ratio was used (also, note change of

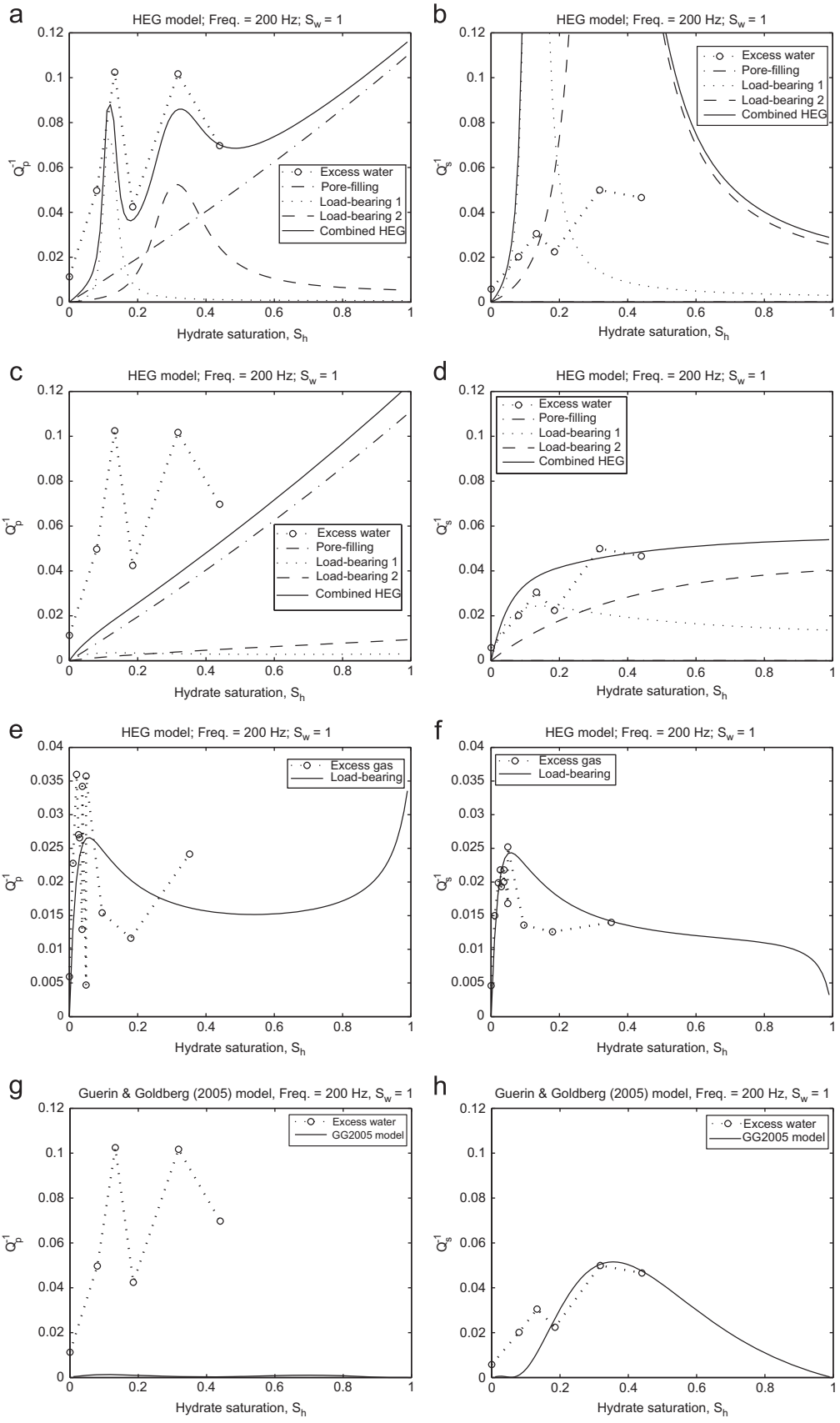

Fig. 6. (a–f) HEG model Q_p^{-1} and Q_s^{-1} results for pore-filling and load-bearing hydrate for disk-shaped inclusions according to Wu (1966) and at a frequency of 200 Hz: (a–d) S_w=1.0 (wet); (e–f) S_w=0.01 (dry). (g–h) Three phase Biot model (Guerin and Goldberg, 2005) predictions. See text for details.

ordinate scale). The results give reasonable estimates of the observed GHRC Q_p^{-1} and Q_s^{-1} values and attenuation peaks, although Q_p^{-1} is slightly underestimated. The load-bearing HEG model suggests a rapid increase in Q_p^{-1} at high S_h, but a rapid drop in Q_s^{-1}.

4. Discussion

Here we compare our experimental attenuation observations (Section 2.3) with data for natural hydrate-bearing sands published in the literature, and our HEG model results (Section 3.2) with published theoretical models.

Guerin and Goldberg (2002) gave sonic log attenuation data in hydrate-bearing sands from the Mallik 2L-38 research well in Canada. They saw a linear increase in Q_p^{-1} and Q_s^{-1} with hydrate saturation S_h with magnitudes at $S_h=0.44$ of $Q_p^{-1}=0.082$ and $Q_s^{-1}=0.140$ (using their least squares regression equations); these values compare to our GHRC values at $S_h=0.44$ of $Q_p^{-1}=0.070$ and $Q_s^{-1}=0.047$. While the GHRC attenuations at seismic frequencies show similar Q_p^{-1} magnitudes, the Q_s^{-1} magnitudes are much lower than the sonic log values. While the Mallik sonic log Q_p^{-1} values are about half those of Q_s^{-1}, the GHRC seismic Q_p^{-1} values are always significantly greater than the Q_s^{-1} values, with a Q_s/Q_p ratio ranging between 1.5 and 3.4. Sonic log values for hydrate-bearing sands in the Nankai Trough from Matsushima (2006) show Q_s/Q_p ratios of about 1.0. Seismic P-wave attenuation magnitudes of $Q_p^{-1}\leq 0.01$ observed by Wood et al. (2000) on Blake Ridge sediments are much lower than the laboratory GHRC values (although for fine grained sediments, not sands). Indeed, it is difficult to compare seismic and sonic log attenuation magnitudes directly with our laboratory results on homogenous specimens because the former are probably influenced by spatial averaging of different (heterogeneous) formations (Bellefleur et al., 2007; Huang et al., 2009), whether due to variations in sediment type (mineralogy, grain packing, cementation), hydrate saturation, hydrate morphology and gas saturation, as well as the effect of measurement frequency and effective pressure. The sonic log tool trace interval is 0.15 m with measurement frequencies of 12 kHz and 2.5 kHz for Q_p^{-1} and Q_s^{-1} respectively, while surface seismic attenuations are averaged over vertical intervals of tens of metres at frequencies between 10 and 100 Hz. Hence, we can only conclude that there are significant differences in attenuation between these two frequency and spatial averaging scales, controlled by attenuation mechanisms yet to be determined.

We adopted a particular theoretical approach, the hybrid HEG model, which involves a somewhat arbitrary combination of model choices, in an attempt to explain the effect of idealised hydrate morphology on our attenuation observations. A possible physical interpretation of the finite inclusion shear modulus that was introduced in Section 3.2 is the idea of partially formed hydrate inclusions in an otherwise solid hydrate matrix. This is similar to the concept of partially frozen ice in a solid ice matrix that was modelled by Leclaire et al. (1994), essentially as a three phase Biot theory (Biot, 1956a,b) for ice, water and mineral grains with no coupling between ice and grains, only between ice and water, and between water and grains. When implemented for hydrate-bearing sands by Guerin and Goldberg (2002), the model predicted attenuation peaks for both P- and S-waves, although at high hydrate saturations $S_h>0.6$; it was unable to predict the steadily rising attenuation at lower hydrate saturations observed on the sonic well logs.

Further development of the three phase Biot model of Leclaire et al. (1994) for hydrate-bearing sediments has been investigated by, for example, Carcione and Tinivella (2000) and Guerin and Goldberg (2005). The latter authors showed that a squirt flow loss mechanism could explain the high P-wave attenuations seen at low hydrate saturations in the Mallik 2L-38 sonic logging dataset, but not the relatively high S-wave attenuations. Guerin and Goldberg (2005) used the BISQ squirt flow model of Dvorkin and Nur (1993) in their implementation, although the validity of the BISQ model at low frequencies is disputed (Marketos and Best, 2010; Pride et al., 2004). Nevertheless, these findings support our alternative approach to implementing squirt flow in hydrate-bearing sediments and, at least qualitatively, our observations of relatively high attenuation at lower hydrate saturations.

We compare our GHRC results to the Guerin and Goldberg (2005) model predictions in Fig. 6g (Q_p^{-1}) and h (Q_s^{-1}), hereafter referred to as the GG2005 model. We found that, even with the incorporation of the BISQ model expressions, the GG2005 model always significantly underestimated the measured P-wave attenuations at 200 Hz, although it gave reasonable estimates of S-wave attenuation. Hence, Fig. 6g and h show the results for the best fit of the GG2005 model to the Q_s^{-1} observations; the most influential free parameters were the permeabilities of the solid frameworks of sand and hydrate grains, respectively. The best fit values were given by the frame permeabilities for sand $\kappa_{s0}=5.0\times10^{-13}\,m^2$ and for hydrate $\kappa_{h0}=1.5\times10^{-10}\,m^2$. All other parameters were kept the same as in Table 1, except for the grain coordination number which was set at the commonly accepted value of 9, and the fluid viscosity was set to 1.8×10^{-3} Pa s as in Guerin and Goldberg (2005). Other parameter values taken from Guerin and Goldberg (2005) were: the inertial coupling coefficients $r_{13}=0$, $r_{12}=0$ and $r_{23}=0$; solid friction coefficient $b_{13}^0=2.2\times10^8$; and coupling shear modules $\mu_{sh0}=44.0\times10^9$ Pa. We conclude from this exercise that the GG2005 model can explain, in part, the S-wave attenuation observations, at least for one of the peaks. Note that the GG2005 model S-wave attenuation is not affected by the addition of the BISQ model. This suggests the dominant S-wave loss mechanism is global viscous, frictional and inertial coupling, as defined by Guerin and Goldberg (2005), between the three phases: hydrate, water and mineral grains.

Overall, the previously reported velocity results (Priest et al., 2005, 2009) and the HEG model results reported here suggest that the three hydrate morphologies (cementing, pore-filling, load-bearing) are not mutually exclusive, so hydrate cement could have a strong influence on velocities while having a negligible influence on attenuation. However, the correspondence between velocities and attenuations requires further investigation, an important consideration for a valid model (Guerin and Goldberg, 2005; Lee, 2007; Waite et al., 2010). Cementation was included in the GG2005 model; like our HEG model results, Guerin and Goldberg (2005) also found it has a negligible effect of attenuation.

5. Conclusions

Laboratory resonant column results on methane hydrate-bearing sand specimens show that seismic P- and S- wave attenuation (Q_p^{-1} and Q_s^{-1}) are sensitive to the hydrate formation process, and by inference to hydrate morphology. We observed a general increase in Q_p^{-1} and Q_s^{-1} with hydrate saturation in water saturated, excess water hydrate sand specimens with magnitudes higher than the attenuations observed in methane gas saturated, excess-gas hydrate sand specimens. Both hydrate morphologies gave rise to attenuation peaks, at hydrate saturations 0.05 (excess-gas) and 0.13, 0.32 (excess water). Attenuation was significantly higher in hydrate-bearing sand than in partially water/methane gas saturated sand.

We modified extant velocity models to predict seismic attenuation in sand caused by viscous squirt flow related to microporous hydrate acting as either grain coating cement, load-bearing grains or pore-filling grains, respectively. Only pore-filling and load-bearing hydrate could predict the levels of P-wave attenuation observed in the laboratory, and only load-bearing hydrate could predict the associated attenuation peaks. Significant S-wave attenuation was predicted for load-bearing hydrate (none for pore-filling hydrate), although it was impossible to reproduce the observed Q_s/Q_p ratios under water saturated conditions using the new model. However, a three phase global fluid flow model was able to predict the S-wave attenuation magnitudes (only one peak), but not the P-wave attenuation magnitudes at a frequency of 200 Hz. It is possible that the other attenuation peak is caused by squirt flow related to load-bearing hydrate.

Overall, we conclude that the observed resonant column attenuations are likely to be the result of a combination of mechanisms associated with different microporous hydrate morphologies. These include squirt flow due to water-filled, low aspect ratio ($\sim 10^{-4}$) pores in the hydrate, possibly disk-like inclusions of partially formed hydrate in solid hydrate, as well as low aspect ratio pores between sand and hydrate grains. The relationship between the observed velocities and attenuations needs further investigation, but suggests that different hydrate morphologies can co-exist and they affect velocity and attenuation to different degrees. Referring to specific model implementations of idealised hydrate morphologies, grain cementing hydrate seems to have the most influence on velocity, while load-bearing hydrate has the most influence on attenuation at hydrate saturations below 0.44. Pore-filling hydrate is only important for P-wave attenuation in saturated sediments.

Acknowledgements

We thank the United Kingdom's Natural Environment Research Council, and Engineering and Physical Sciences Research Council (EPSRC Grant EP/D035996/1), for funding and the helpful comments of the reviewers.

Appendix A. Supporting information

Supplementary data associated with this article can be found in the online version at http://dx.doi.org/10.1016/j.epsl.2013.02.033.

References

Bellefleur, G., Riedel, M., Brent, T., Wright, F., Dallimore, S.R., 2007. Implication of seismic attenuation for gas hydrate resource characterization, Mallik, Mackenzie Delta, Canada. J. Geophys. Res. 112 (B10311), http://dx.doi.org/10.1029/2007JB004976.

Berryman, J.G., 1995. Mixture theories for rock properties. In: Ahrens, T.J. (Ed.), Rock Physics & Phase Relations: A Handbook of Physical Constants. American Geophysical Union, Washington, DC, pp. 205–228.

Best, A.I., McCann, C., 1995. Seismic attenuation and pore-fluid viscosity in clay-rich reservoir sandstones. Geophysics 60, 1386–1397.

Best, A.I., Priest, J.A., Clayton, C.R.I., 2010. A resonant column study of the seismic properties of methane-hydrate-bearing sand. In: Riedel, M., Willoughby, E.C., Chopra, S. (Eds.), Geophysical Characterization of Gas Hydrates. Society of Exploration Geophysicists, pp. 337–346.

Biot, M.A., 1956a. Theory of propagation of elastic waves in a fluid-saturated porous solid. II. Higher frequency range. J. Acoust Soc Am 28, 179–191.

Biot, M.A., 1956b. Theory of propagation of elastic waves in a fluid-saturated porous solid: I. Low-frequency range. J. Acoust Soc Am 28, 168–178.

Birch, F., 1961. The velocity of compressional waves in rocks to 10 Kilobars, Part 2. J. Geophys. Res. 66, 2199–2224.

Carcione, J.M., Tinivella, U., 2000. Bottom-simulating reflectors: sesimic velocities and AVO effects. Geophysics 65, 54–67.

Chand, S., Minshull, T.A., Priest, J.A., Best, A.I., Clayton, C.R.I., Waite, W.F., 2006. An effective medium inversion algorithm for gas hydrate quantification and its application to laboratory and borehole measurements of gas hydrate bearing sediments. Geophys. J. Int. 166, 543–552, http://dx.doi.org/10.1111/j.1365-246X.2006.03038.x.

Clayton, C.R.I., Priest, J.A., Best, A.I., 2005. The effects of disseminated methane hydrate on the dynamic stiffness and damping of a sand. Géotechnique 55, 423–434.

Clayton, C.R.I., Priest, J.A., Rees, E.V.L., 2010. The effects of hydrate cement on the stiffness of some sands. Geotechnique 60, 435–445, http://dx.doi.org/10.1680/geot.2010.60.6.435.

Dvorkin, J., Nur, A., 1993. Dynamic poro-elasticity: a unified model with the squirt and the Biot mechanisms. Geophysics 58, 523–533.

Dvorkin, J., Nur, A., Uden, R., Taner, T., 2003. Round table—rock physics of a gas hydrate reservoir. Leading Edge 22, 842–847.

Dvorkin, J., Nur, A., Yin, H., 1994. Effective properties of cemented granular material. Mech. Mater. 18, 351–366.

Dvorkin, J., Prasad, M., Sakai, A., Lavoie, D., 1999. Elasticity of marine sediments: rock physics modeling. Geophys. Res. Lett. 26, 1781–1784.

Dvorkin, J., Uden, R., 2004. Interpreter's corner—seismic wave attenuation in a methane hydrate reservoir. Leading Edge 23, 730–732.

Ecker, C., Dvorkin, J., Nur, A., 1998. Sediments with gas hydrates: internal structure from seismic AVO. Geophysics 63, 1659–1669.

Ecker, C., Dvorkin, J., Nur, A.M., 2000. Estimating the amount of gas hydrate and free gas from marine seismic data. Geophysics 65, 565–573.

Gassmann, F., 1951. Elastic waves through a packing of spheres. Geophysics 16, 673–685.

Guerin, G., Goldberg, D., 2002. Sonic waveform attenuation in gas hydrate-bearing sediments from the Mallik 2L-38 research well, Mackenzie Delta, Canada. J. Geophys. Res. 107, B52088, http://dx.doi.org/10.1029/2001JB000556.

Guerin, G., Goldberg, D., 2005. Modeling of acoustic wave dissipation in gas hydrate-bearing sediments. Geochem. Geophys. Geosyst. 6, Q07010, http://dx.doi.org/10.1029/2005GC000918.

Huang, J.W., Bellefleur, G., Milkereit, B., 2009. Seismic modeling of multidimensional heterogeneity scales of Mallik gas hydrate reservoirs, Northwest Territories of Canada. J. Geophys. Res. Solid Earth 114, B07306, http://dx.doi.org/10.1029/2008jb006172.

Johnston, D.H., Toksöz, M.N., Timur, A., 1979. Attenuation of seismic waves in dry and saturated rocks: II. Mechanisms. Geophysics 44, 691–711.

Kuhs, W.F., Genov, G., Goreshnik, E., Zeller, A., Techmer, K.S., Bohrmann, G., 2004. The impact of porous microstructures of gas hydrates on their macroscopic properties. Int. J. Offshore Polar Eng. 14, 305–309.

Leclaire, P., Cohen-Ténoudji, F., Aguirre-Puente, J., 1994. Extension of Biot's theory of wave propagation to frozen porous media. J. Acoust. Soc. Am. 96, 3753–3768.

Lee, M.W., 2002. Biot–Gassmann theory for velocities of gas hydrate-bearing sediments. Geophysics 67, 1711–1719, http://dx.doi.org/10.1190/1.1527072.

Lee, M.W., 2007. Velocities and attenuations of gas hydrate-bearing sedments, Scientific Investigations Report 2007-5264. US Geological Survey, Reston, Virginia, USA, p. 11.

Leurer, K.C., 1997. Attenuation in fine-grained marine sediments: extension of the Biot-Stoll model by the "effective grain model" (EGM). Geophysics 62, 1465–1479.

Leurer, K.C., Brown, C., 2008. Acoustics of marine sediment under compaction: binary grain-size model and viscoelastic extension of Biot's theory. J. Acoust. Soc. Am. 123, 1941–1951, http://dx.doi.org/10.1121/1.2871839.

Marketos, G., Best, A.I., 2010. Application of the BISQ model to clay squirt flow in reservoir sandstones. J. Geophys. Res. 115, http://dx.doi.org/10.1029/2009JB006495.

Matsushima, J., 2006. Seismic wave attenuation in methane hydrate-bearing sediments: vertical seismic profiling data from the Nankai Trough exploration well, offshore Tokai, central Japan. J. Geophys. Res. 111, B10101, http://dx.doi.org/10.1029/2005JB004031.

Mavko, G., Mukerji, T., Dvorkin, J., 1998. The Rock Physics Handbook: Tools for Seismic Analysis in Porous Media. Cambridge University Press, Cambridge.

Pratt, R.G., Hou, F., Bauer, K., Weber, M., 2005. Waveform tomography images of velocity and inelastic attenuation from the Mallik 2002 crosshole seismic surveys. In: Dallimore, S.R., Collett, T.S. (Eds.), Scientific Results from the Mallik 2002 Gas Hydrate Production Research Well Program, Mackenzie Delta, Northwest Territories. Geological Survey of Canada, Canada, pp. 14.

Pride, S.R., Berryman, J.G., Harris, J.M., 2004. Seismic attenuation due to wave-induced flow. J. Geophys. Res. 109, B01201, http://dx.doi.org/10.1029/2003JB002639.

Priest, J.A., 2004. The Effect of Methane Gas Hydrate on the Dynamic Properties of Sand. Ph.D. Thesis. University of Southampton, Southampton.

Priest, J.A., Best, A.I., Clayton, C.R.I., 2005. A laboratory investigation into the seismic velocities of methane gas hydrate-bearing sand. J. Geophys. Res. B Solid Earth 110, B04102, http://dx.doi.org/10.1029/2004JB003259.

Priest, J.A., Best, A.I., Clayton, C.R.I., 2006. Attenuation of seismic waves in methane gas hydrate-bearing sand. Geophys. J. Int. 164, 149–159, http://dx.doi.org/10.1111/j.1365-246X.2005.02831.X.

Priest, J.A., Rees, E.V.L., Clayton, C.R.I., 2009. Influence of gas hydrate morphology on the seismic velocities of sands. J. Geophys. Res. 114, B11205, http://dx.doi.org/10.1029/2009JB006284.

Rees, E.V.L., 2009. The Effect of Natural and Synthesised Methane Gas Hydrate on the Stiffness of Some Sediments. Ph.D. Thesis. University of Southampton, United Kingdom, Southampton.

Riedel, M., Willoughby, E.C., Chopra, S., 2010. Gas hydrates—geophysical exploration techniques and methods. In: Riedel, M., Willoughby, E.C., Chopra, S. (Eds.), Geophysical Characterization of Gas Hydrates. Society of Exploration Geophysicists, Tulsa, Oklahoma, pp. 1–22.

Waite, W.F., Santamarina, J.C., Cortes, D.D., Dugan, B., Espinoza, D.N., Germaine, J., Jang, J., Jung, J.W., Kneafsey, T.J., Shin, H., Soga, K., Winters, W.J., Yun, T.S., 2010. Physical properties of hydrate-bearing sediments. Rev. Geophys. 47 (RG4003), 4001–4038.

Walsh, J.B., 1969. New analysis of attenuation in partially melted rock. J. Geophys. Res. 74, 4333–4337.

Westbrook, G.K., Chand, S., Rossi, G., Long, C., Bünze, S., Camerlenghi, A., Carcione, J.M., Dean, S., Foucher, J.-P., Flueh, E., Geid, D., Haacke, R.R., Madrussani, G., Mienert, J., Minshull, T.A., Nouzé, H., Peacock, S., Reston, T.J., Vannestee, M., Zillmer, M., 2008. Estimation of gas hydrate concentration from multi-component seismic data at sites on the continental margins of NW Svalbard and the Storegga region of Norway. Mar. Pet. Geol. 25, 744–758.

Westbrook, G.K., Thatcher, K.E., Rohling, E.J., Piotrowski, A.M., Paelike, H., Osborne, A.H., Nisbet, E.G., Minshull, T.A., Lanoiselle, M., James, R.H., Huehnerbach, V., Green, D., Fisher, R.E., Crocker, A.J., Chabert, A., Bolton, C., Beszczynska-Moeller, A., Berndt, C., Aquilina, A., 2009. Escape of methane gas from the seabed along the West Spitsbergen continental margin. Geophys. Res. Lett. 36, L15608, http://dx.doi.org/10.1029/2009gl039191.

Winkler, K.W., Nur, A., 1979. Pore fluids and seismic attenuation in rocks. Geophys. Res. Lett. 6, 1–4.

Wood, W.T., Holbrook, W.S., Hoskins, H., 2000. In situ measurements of P-wave attenuation in the methane hydrate- and gas-bearing sediments of the Blake Ridge. In: Proceedings of the Ocean Drilling program, Scientific Results, vol. 164, pp. 265–272.

Wu, T.T., 1966. The effect of inclusion shape on the elastic moduli of a two phase material. Int. J. Solids Struct. 2, 1–8.

Yun, T.S., Francisca, F.M., Santamarina, J.C., Ruppel, C., 2005. Compressional and shear wave velocities in uncemented sediment containing gas hydrate. Geophys. Res. Lett. 32, L10609–L10613.